PHYSICS

Exploiting compositional disorder in collectives of light-driven circle walkers

Frank Siebers, Ashreya Jayaram, Peter Blümler, Thomas Speck*

Emergent behavior in collectives of "robotic" units with limited capabilities that is robust and programmable is a promising route to perform tasks on the micro and nanoscale that are otherwise difficult to realize. However, a comprehensive theoretical understanding of the physical principles, in particular steric interactions in crowded environments, is still largely missing. Here, we study simple light-driven walkers propelled through internal vibrations. We demonstrate that their dynamics is well captured by the model of active Brownian particles, albeit with an angular speed that differs between individual units. Transferring to a numerical model, we show that this polydispersity of angular speeds gives rise to specific collective behavior: self-sorting under confinement and enhancement of translational diffusion. Our results show that, while naively perceived as imperfection, disorder of individual properties can provide another route to realize programmable active matter.

INTRODUCTION

Autonomous microrobots that perform useful tasks have been a popular and scientific vision (*1*). At the (sub)microscale, these machines will need to overcome a number of physical limitations that severely restrict computational capabilities and the amount of information that can be gathered and processed. Moreover, in aqueous environments, thermal fluctuations cannot be neglected (*2*, *3*). Single units thus operate on the basis of incomplete and noisy input and will be error prone. The question of how collectives of many motile units working together can overcome these limitations and lead to reproducible and robust emergent behavior has motivated intensive research based largely on macroscopic model systems, such as "kilobots" (*4*), with the capability to communicate (*5*).

On smaller scales, directed motion of colloidal particles can be achieved through different mechanisms including thermophoresis (*6*), diffusiophoresis (*7*, *8*), photocatalysis (*9*, *10*), induced-charge electrophoresis (*11*), and Quincke rotation (*12*–*14*). On the other hand, the biological world exploits self-propulsion to, inter alia, explore surroundings for nutrition (*15*, *16*) and migrate to more conducive environments (*17*). A rapidly growing body of studies has demonstrated that physical interactions (both steric and hydrodynamic) are sufficient for the emergence of a wealth of collective dynamic states such as clustering (*7*, *9*) and swarming (*18*) in microscopic active systems (*19*). These states often display long-ranged correlations and are highly sensitive to boundaries and external perturbations. The tendency of active particles to accumulate at boundaries (*20*–*22*) promotes phenomena like rectification (*23*, *24*) and trapping (*18*, *25*). Developing strategies to translate these properties into the rational design of adaptable and programmable behavior is of particular interest for soft robotics (*26*, *27*).

Well-controlled minimal model systems, both experimental and theoretical, are essential to expose and systematically study underlying universal principles. Here, we study the collective behavior of commercially available light-driven walkers (Fig. 1A and movie S1) that emerges from physical interactions with each other and with boundaries (*21*, *22*, *28*) in the absence of direct communication. These walkers are propelled forward by mechanical vibrations that are transmitted through flexible "legs" that are inclined backward [similar to bristle-bots (*29*)]. Energy is provided through a strong light source that drives a vibration motor through a photovoltaic cell. Walkers have a roughly elliptical shape and align their orientations during contact. Slight differences in the length, shape, and stiffness of the legs lead to circular trajectories with a characteristic radius that is different for each walker, realizing a novel type of "polydispersity" only accessible to driven active particles. We link the dynamics of walkers to the microscopic model of "dry" active Brownian motion (*30*, *31*). In contrast to other macroscopic model systems of self-propelled particles in which mass (hence, inertia) might play a role (*32*–*37*), these walkers are well described by overdamped (noninertial) equations of motion. Instead of explicitly modeling the ellipsoidal shape of these walkers (*38*, *39*), we introduce an effective Vicsek-like alignment (*40*) that acts on their orientations. The interplay of excluded-volume interactions, alignment, and polydisperse angular speeds results in a selective enhancement of translation diffusion over monodisperse collectives. We demonstrate that this enhancement can be exploited in confinement to sort walkers on the basis of their angular speeds.

RESULTS

Single walker dynamics

We study 20 light-driven walkers bounded by a circular confinement illuminated from above. The resulting light intensity is nonuniform but above the motion threshold of the walkers, resulting in an individual but constant propulsion speed within the whole arena (details in Materials and Methods). The length of walkers is $a \simeq 4.9$ cm, and the radius of the arena is $R_0 = 35$ cm $\simeq 7.14a$. To characterize individual walkers, we record trajectories within the circular confinement and extract their positions and orientations (Fig. 1B). In Fig. 1C, four such trajectories are plotted for the same walker, which show considerable variation. Though walkers get trapped at the boundary because of their directed motion, they also spend a considerable time away from the boundary. To remove the effect of confinement and construct effectively

Institut für Physik, Johannes Gutenberg-Universität Mainz, Staudingerweg 7-9, 55128 Mainz, Germany.
*Corresponding author. Email: thomas.speck@uni-mainz.de

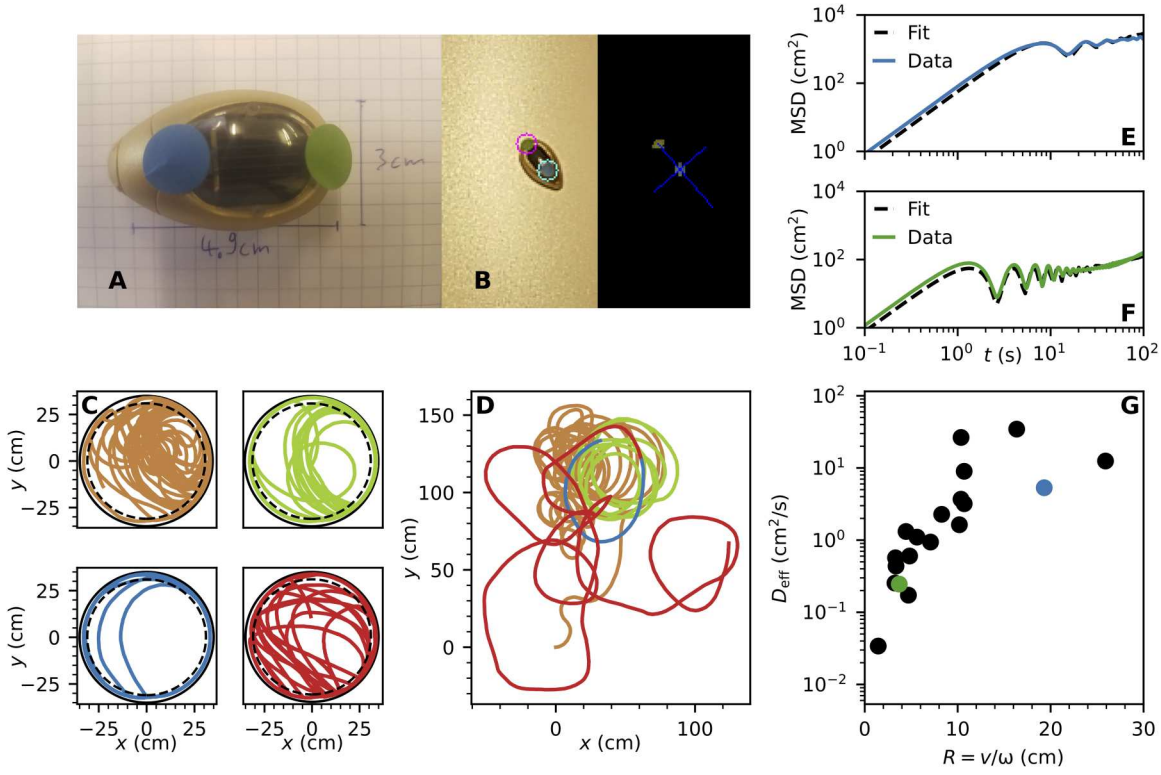

Fig. 1. Light-driven walkers. (**A**) Picture of a single walker from above. The colored dots are attached to allow easy tracking of position and orientation. (**B**) Image of a single walker before (left) and after (right) processing. (**C**) Recorded raw trajectories within the circular confinement (four runs of the same walker). The dashed line delineates the inner area, from which we extract trajectory sections. (**D**) Unbounded trajectories obtained by concatenation of these trajectory sections. (**E** and **F**) MSD for two different walkers comparing measurement and model prediction. (**G**) From the fitted model parameters, we plot the translational diffusion coefficient D_{eff} versus the circle radius $R = v/|\omega|$. The colored points correspond to the two walkers shown in (E) and (F).

unbounded trajectories, we define an inner area (dashed line in Fig. 1C) bounded by a circle of radius $R_i = 31$ cm. Every time a walker intersects this circle, the trajectory is cut and the sections outside the inner area are discarded. These disjoint sections are rotated so that they align at their initial and final orientations. They are then translated and concatenated to form a single long trajectory; cf. Fig. 1D. We collect up to 158 trajectory sections per walker with a total time of at least 600 s.

We calculate the mean-squared displacement $\mathrm{MSD}(t) = \langle|\mathbf{r}(t) - \mathbf{r}(0)|^2\rangle$ of the unbounded position $\mathbf{r}$ by averaging over these trajectories. As shown in Fig. 1 (E and F) for two walkers, there is considerable variation in dynamical properties between individual walkers. Not aiming to capture every detail, we describe the dynamics of the individual walkers with the following minimal model (*29*).

$$\dot{\mathbf{r}} = v\begin{pmatrix}\cos\varphi\\ \sin\varphi\end{pmatrix},\quad \dot{\varphi} = \omega + \sqrt{2/\tau}\eta \qquad (1)$$

Each walker is characterized by an individual propulsion speed v and angular speed ω. Nondeterministic effects on the orientation φ (the angle enclosed with an arbitrary but fixed direction) are modeled as rotational diffusion through a stochastic differential equation (*41*). The strength of the noise is determined by the correlation time τ and η is a random noise with zero mean and correlations $\langle\eta(t)\eta(t')\rangle = \delta(t - t')$. Without rotational noise ($\tau \to \infty$), the unperturbed trajectories would be circles of radius $R = v/|\omega|$.

From the model (Eq. 1), an analytic expression for the MSD can be obtained (Eq. 3 in Materials and Methods). In Fig. 1 (E and F), we also show fits to the measured MSD(t). Because of rotational diffusion, in the long-time limit, each walker undergoes purely diffusive motion with translational diffusion coefficient $D_{\mathrm{eff}} = \frac{v^2\tau}{2[1+(\omega\tau)^2]}$. A second length scale is the distance $\ell = \sqrt{D_{\mathrm{eff}}\tau}$ the center of the walker's circular trajectory diffuses over the time the orientational correlations persist. For $\omega\tau \gg 1$, this length reduces to $\ell \approx R/\sqrt{2}$ with $D_{\mathrm{eff}} \approx R^2/(2\tau)$. We observe good agreement between data and the model prediction using individual parameters that differ for distinct walkers. Most noticeable is the broad distribution of angular speeds ranging from right- and leftward circling to almost straight motion. Figure 1G shows the radii of the circular trajectory R and the translational diffusion coefficient D_{eff} for the 20 walkers.

Collision dynamics

To study the collective behavior of many walkers, we require a model for their interactions. To this end, we perform many short experiments with two walkers that collide, glide along each other, and detach. From their positions and orientations, we calculate the center-to-center distance $\Delta r = |\mathbf{r}_k - \mathbf{r}_l|$ by defining the "center" as the center of the major axis and the relative angular speed $\hat{\omega}_a(t) = (\dot{\varphi}_k - \dot{\varphi}_l) - (\omega_k - \omega_l)$ with respect to the frame of reference rotating with angular speed $\omega_k - \omega_l$ of walkers with indices k and l. Both curves are plotted in Fig. 2 as a function of

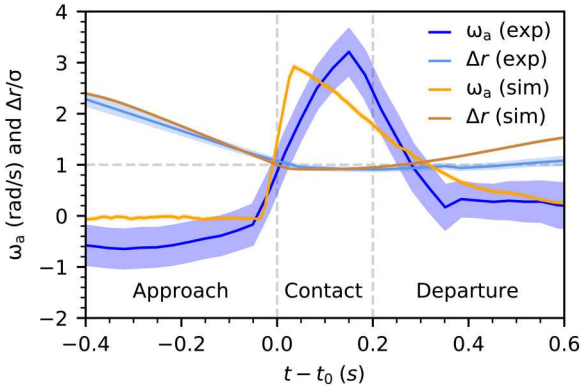

Fig. 2. The model captures the collision dynamics. Evolution of relative angular speed ω_a and distance Δr. Shown is the average over all recorded collision trajectories (shifted by the contact time t_0) with the shaded area indicating the statistical standard error. Also shown are simulation results using the schematic alignment interaction Eq. 2. The vertical dashed lines indicate the data range from which we calculate the alignment strength κ, starting from when the distance between walkers Δr has fallen below the alignment range σ ($\sigma \simeq 4$ cm for experiments and $\sigma = 1.25a$ in simulations).

time. The average $\langle \Delta r(t) \rangle$ decreases as the two walkers approach, plateaus at the alignment range σ during contact, and increases as they part ways. This naturally defines three stages: approach, contact, and departure. We define t_0 as the time at which walkers come in contact and shift all trajectories by it before averaging. The orientations of both walkers align during contact; this is visible in the nonmonotonic nature of $\omega_a(t) = \langle \hat{\omega}_a(t) \rangle$ that peaks shortly after contact. To model this behavior, we extend Eq. 1 to include a schematic alignment of the form

$$\dot{\varphi}_k = \omega_k + \sqrt{2/\tau}\eta_k + \begin{cases} \frac{\kappa a^2}{\pi\sigma^2\tau}\sum_l \sin(\varphi_l - \varphi_k) & (\Delta r \le \sigma) \\ 0 & (\Delta r > \sigma) \end{cases} \quad (2)$$

with a torque proportional to $\sin(\varphi_l - \varphi_k)$ as long as both walkers are in contact. The torque vanishes if the two walkers move in parallel, and it is maximal if they are oriented perpendicular to each other. The strength of this aligning torque is determined by κ. Further details about the model are presented in the Supplementary Materials. Such a schematic alignment is sufficient to capture the emerging large-scale behavior (*42*), which does not depend on the exact shape of the walkers. Previously, this model has been studied numerically for a binary mixture with angular speeds $\pm\omega$ (*43*). Moreover, for $v = 0$ it reduces to the off-lattice variation of the noisy Kuramoto model (*44*). The dimensionless alignment strength κ is estimated from a hundred isolated collisions of two walkers (movie S2). We calculate $\Delta\varphi = \varphi_k - \varphi_l$ and the instantaneous angular speed $\hat{\omega}_a$ for each frame within 0.2 s after contact (vertical dashed lines in Fig. 2). From them, we determine $\hat{\kappa} = \pi(\sigma/a)^2\hat{\omega}_a\tau/(2\sin\Delta\varphi)$. The average $\kappa = \langle\hat{\kappa}\rangle$ over all frames and all collisions yields $\kappa = 39.6 \pm 4.4$.

Numerical model

We now transfer the experimental results to a numerical model to gain insights into larger collectives. To focus on the role of different angular speeds, we use a simplified model in which walkers have the same speed v and correlation time τ but different angular speeds ω_k, which we draw from a bimodal distribution (plotted in Materials and Methods). Note that such a distribution of angular speeds differs from polydisperse persistence lengths (either through speed or correlation time, or both) (*45*). Here, we study constant persistence in the presence of polydisperse angular speeds ω_k.

In all simulations, we set the alignment strength $\kappa = 40$ for all walkers and numerically integrate Eq. 2. We additionally introduce a short-ranged repulsive and isotropic force between walkers to model the excluded volume of discs with diameter a (Materials and Methods). The resulting curves for $\langle\omega_a(t)\rangle$ and $\langle\Delta r(t)\rangle$ are plotted in Fig. 2 and show reasonable agreement with the experimental data. The alignment model overestimates ω_a at impact, but the overall change in rotation speed while in contact is very similar in simulations and experiments. Representative trajectories of a few walkers shown in Fig. 3 demonstrate qualitative agreement between simulations and experiments.

Enhanced translational diffusion

We now perform numerical simulations of $N = 1000$ interacting walkers based on the model (Eq. 2) using parameters extracted from the experiments. The simulations are performed in a square box with periodic boundary conditions at an intermediate global packing fraction $\phi = 0.24$. Previous investigations of walkers with uniform ω in a periodic system have reported clustering into "microflocks" (*46*) and a hyperuniform phase (in the absence of alignment) (*47*), which has been recently observed in experiments with pear-shaped Quincke rollers (*48*). In our system, the different preferred radii $R_k = v/\omega_k$ counteract the formation of these structures, and our system remains homogeneous at $\phi = 0.24$ (movie S3). To understand why disorder suppresses clustering, consider two walkers in contact experiencing torques that align their orientations. Compared to walkers with identical ω, different angular speeds move them apart quicker, thereby reducing their contact time. This effect hinders cluster formation and, on first impression, seems to counteract collective behavior.

Conversely, in Fig. 4, we show that this is not the case and that the heterogeneity of angular speeds produces an enhanced diffusion depending on the individual angular speed ω_k. Figure 4 (A and B) shows the impact of heterogeneity on trajectories of individual walkers: For identical angular speeds, trajectories remain circular (Fig. 4A), whereas for distributed angular speeds (Fig. 4B), trajectories becomes irregular and spatially extended. In the latter case, collisions predominantly occur between walkers with similar orientations; consequently, circular trajectories are stable even in

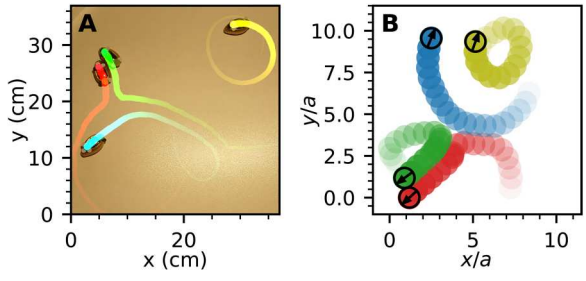

Fig. 3. Simulated trajectories agree with experiments. (**A**) Experimental snapshot of an assembly of walkers with their path traveled indicated by fading color. (**B**) Snapshot from a low-density simulation (showing four of $N = 15$ walkers with packing fraction $\phi \simeq 0.04$) in circular confinement that emulates the experimental setup.

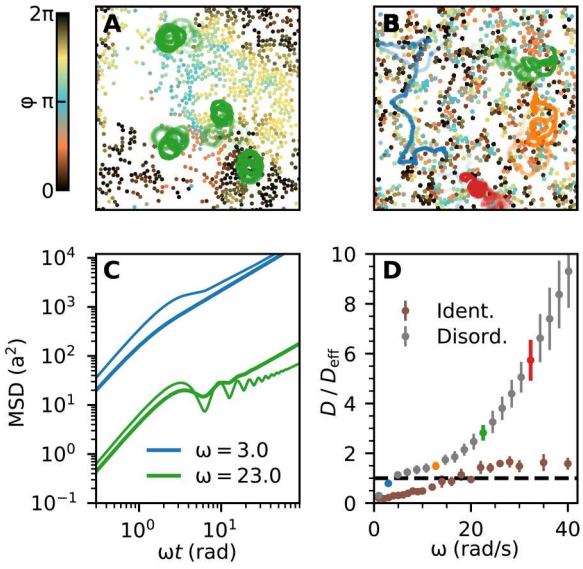

Fig. 4. Polydispersity of angular speeds enhances translational diffusion. Simulation snapshots of $N = 1000$ walkers at global packing fraction $\phi = 0.24$ using periodic boundary conditions: (**A**) Identical angular speed ($\omega\tau = 23$) and (**B**) distributed speeds. Colors denote walker orientations and fading lines show example trajectories of four walkers with $\omega\tau$= 3 (blue), 13 (orange), 23 (green), and 33 (red). (**C**) MSD averaged over all walkers with angular speed ω for two values (thick lines). The thin lines show Eq. 3 for noninteracting walkers. (**D**) Reduced translational diffusion coefficient D/D_{eff} as a function of angular speed ω. MSDs are calculated for all walkers with $\omega_k \in [\omega - 1, \omega + 1)$. Colored symbols correspond to curves in other panels. For comparison, we also show the diffusion coefficient for a system of identical walkers ($\omega_k = \omega$).

the presence of interactions. In contrast, for distributed angular speeds, collisions lead to deflections that effectively increase the radius R.

To show that the strength of this effect depends on the intrinsic angular speed, we bin walkers with similar ω_k and calculate their MSD. In Fig. 4C, for interacting walkers, we show the result for one small and one large angular speed. To assess the effect of interactions, we also plot the free MSD (Eq. 3). We find that for small angular speeds ω_k (large R_k), oscillations are strongly suppressed, indicating that the regime of normal diffusion is reached quickly. Comparable to active particles with $\omega = 0$ (*39*), the long-time diffusion is reduced because of a reduction of the effective speed due to collision. In contrast, for large ω_k, the MSD increases at late times when compared to the noninteracting and uniform systems (cf. green trajectory in Fig. 4A). In Fig. 4D, we plot the ratio of the long-time diffusion coefficient D with respect to D_{eff}. Ensembles of identical walkers also experience enhanced diffusion, but this increase is moderate (less than a factor of 2), whereas the enhancement for polydisperse walkers is almost 10-fold.

Confinement induces sorting

To explore how the distribution of angular speeds affects the collective behavior of walkers in the presence of boundaries, we return to the circular confinement of the experiments. The walkers experience additional aligning (Eq. 9 in Materials and Methods) and excluded-volume (Eq. 6 in Materials and Methods) interactions due to the presence of the wall. Figure 5A shows a representative simulation snapshot of the system. As known from active Brownian particles, walkers accumulate at the confining wall with average polarization along the outward normal vector. The reason is the

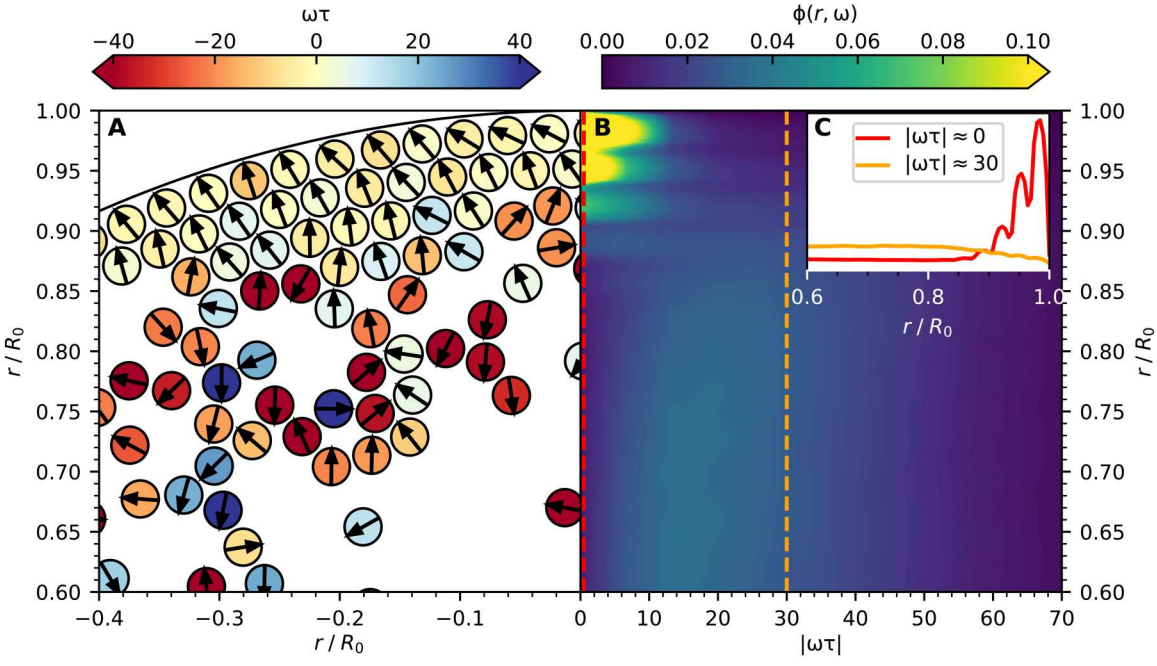

Fig. 5. Confinement induces sorting of walkers. (**A**) Simulation snapshot of $N = 1000$ walkers at global packing fraction $\phi = 0.24$. Colors indicate the intrinsic rotation speeds with $\tau = 19.3$ s (color bar) and arrows the orientations of individual walkers. (**B**) Local packing fraction $\phi(r, \omega)$ at normalized distance r/R_0 from the center of the confinement and absolute angular speed $|\omega|$ calculated in bins of sizes 0.01 and 5 respectively. The inset (**C**) shows the packing fractions for the two angular speeds indicated in (B) by the dashed lines.

persistence of motion, which traps particles for a time ∼τ until their orientations point into the bulk, allowing them to escape before persistence drives them back to the confining wall (*21*, *22*, *28*).

Looking closer, we find that walkers with small $|\omega_k|$ aggregate preferably at the wall forming two to three close-packed layers, while the disordered bulk is mostly composed of walkers with large $|\omega_k|$ independent of their rotation direction. This is confirmed by plotting the local packing fraction $\phi(r, \omega)$ shown in Fig. 5B. Walkers with small $|\omega_k|$ aggregate at the wall and are therefore depleted in the bulk ($r/R_0 \lesssim 0.9$, cf. inset). On the other hand, a large intrinsic angular speed dominates over the diffusive reorientation, and walkers point away from the wall quickly. From the balance of torques in Eq. 2, one finds a critical angular speed $\omega_c\tau \simeq 4\kappa\phi/\pi \simeq 12$ above which the alignment is insufficient to overcome the intrinsic rotation. In Fig. 5B, we see that, indeed, walkers with $|\omega_k| \gtrsim \omega_c$ are effectively repelled by the wall and migrate to the bulk. In Fig. 6, we demonstrate that in addition, alignment is crucial for sorting walkers on the basis of their angular speeds. If alignment is turned off ($\kappa = 0$ but still with volume exclusion), we observe a uniform spatial distribution of walkers (Fig. 6A), whereas the same distribution of angular speeds, but now in the presence of alignment, leads to aggregation and spatial sorting of walkers with different angular speeds (Fig. 6B). This effect requires explicit walls different from the bulk segregation of left/right rotating robots (*34*, *49*). While the torque due to the confinement aligns walkers tangentially, the competing interparticle alignment interactions promote aggregation by orienting walkers normal to the confinement.

DISCUSSION

Deliberately exploiting physical interactions and imperfections instead of engineering communication protocols to carefully control (and often avoid) interactions is an emerging paradigm in collectives of robotic units. It allows to exploit the robust collective behaviors found in a wide range of physical and biological active matter systems (*19*) toward the implementation of adaptable and programmable behavior. Here, we have studied a model system of light-driven walkers that bridges the gap between well-studied active matter models and robotics. We have gained first insights into the role of a distribution of angular speeds. The intricate interplay of alignment and disorder leads to collectively enhanced diffusion and spatial inhomogeneity of individual properties under confinement. The preferential aggregation of straight walkers at walls could be exploited by designing traps (*25*) but also to tune properties of systems with deformable boundaries such as vesicles (*50*–*52*) and the steering of deformable soft superstructures (*53*). An intriguing perspective is to study the influence of underlying parameter distributions in the presence of time-dependent and inhomogeneous fields (realizable here through the light profile) with the aim to switch collective modes (*54*).

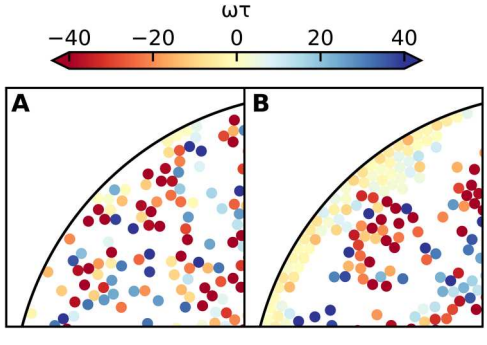

Fig. 6. Alignment is crucial for sorting. Simulation snapshots of walkers (**A**) without alignment ($\kappa = 0$) and (**B**) with alignment ($\kappa = 40$) under confinement at packing fraction $\phi = 0.24$. Color scale as in Fig. 5A denoting the angular speed ω.

MATERIALS AND METHODS

Setup and light profile

We have constructed a circular arena made of white, medium-density fiberboard as surface and a bent cover strip as border with radius $R_0 = 35$ cm. For illumination, we use two halogen bulbs (Tungsram55060 Lampada Alogena 230v 1000w GX 6,35-25) centered 71 cm above. The lamp case and the camera are fixed on a movable mount placed on a rectangular metal bar frame. Figure 7 shows the measured light intensity inside the arena and its distance dependence together with a Gaussian fit. Walkers were found to move only if the light intensity is above a threshold of 20.6 klx.

Mean-squared displacement

For the model (see Eq. 1), the MSD can be calculated analytically and reads (*55*)

$$\mathrm{MSD}(t) = \langle |\, \mathbf{r}(t) - \mathbf{r}(0)\,|^2 \rangle = \frac{2(v\tau)^2}{1+(\omega\tau)^2} \times \left\{ \frac{t}{\tau} - \frac{e^{-t/\tau}}{1+(\omega\tau)^2}\left[2\omega\tau \sin \omega t - \left[1-(\omega\tau)^2\right]\cos \omega t\right] - \frac{1-(\omega\tau)^2}{1+(\omega\tau)^2} \right\} \quad (3)$$

The short-time expansion yields ballistic motion, $\mathrm{MSD} = (vt)^2$. In the limit of long times, we find diffusive behavior with $\mathrm{MSD}(t \to \infty) = \frac{2v^2\tau}{1+(\omega\tau)^2} t = 4D_{\mathrm{eff}} t$.

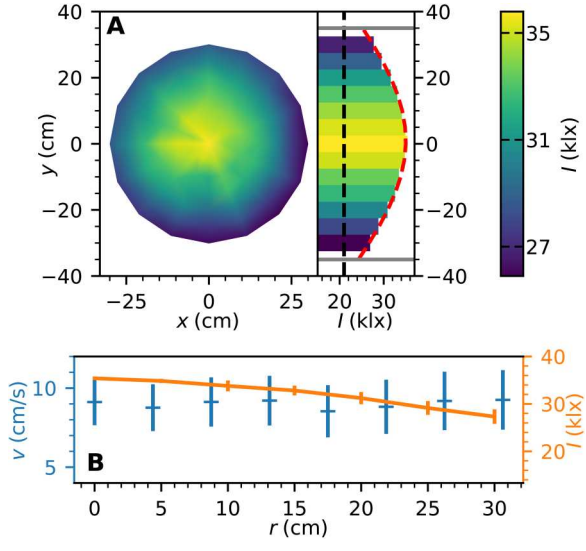

Fig. 7. Light profile measured within the confinement. (**A**) Local intensity on the left and binned data on the right. The radial light intensity is above the motion threshold (black dashed line) within the arena (gray lines) and follows a Gaussian distribution (red dashed line). (**B**) Propulsion speed v and light intensity I at distance r to the arena center.

Simulations

Figure 8 shows the distribution of model parameters for the different walkers. In Fig. 8A, we plot the histogram of the magnitude $|\omega|$. To capture the spreading of angular speeds in simulations, we use the bimodal distribution

$$p(\omega) = \frac{1}{2\sqrt{2\pi}\sigma_\omega}\left[e^{-\frac{1}{2}\frac{(\omega-\mu_\omega)^2}{\sigma_\omega^2}} + e^{-\frac{1}{2}\frac{(\omega+\mu_\omega)^2}{\sigma_\omega^2}}\right] \quad (4)$$

of two symmetric normal distributions centered at $\mu_\omega\tau = 22$ and with SD $\sigma_\omega = 1.2\mu_\omega$. In Fig. 8B, we plot the fitted propulsion speeds, which we represent by a constant speed $v = 60\frac{a}{\tau}$ in the simulations throughout. Figure 8C shows the orientational correlation times divided by their mean $\tau = \langle\tau_k\rangle \simeq 19.3$ s. For simplicity, in the simulations, we use a uniform τ as the unit of time.

To study the collective behavior of walkers, we simulate $N = 1000$ walkers in a domain of area A at global packing fraction $\phi = N\pi\left(\frac{a}{2}\right)^2/A = 0.24$ (if not stated otherwise). To account for excluded volume, we use the short-range repulsive Weeks-Chandler-Andersen (WCA) (*56*) potential

$$U_{\mathrm{WCA}}(r) = \begin{cases} 4\varepsilon\left[\left(\frac{a}{r}\right)^{12} - \left(\frac{a}{r}\right)^{6}\right] + \varepsilon, & r \le 2^{1/6}a \\ 0, & r > 2^{1/6}a \end{cases} \quad (5)$$

with $\varepsilon = 100\frac{a^2}{\tau}$. Walkers also interact with the confinement through the WCA potential

$$U_{\mathrm{con}}(r) = \begin{cases} 4\varepsilon\left[\left(\frac{a/2}{R-r}\right)^{12} - \left(\frac{a/2}{R-r}\right)^{6}\right] + \varepsilon, & r \ge R - 2^{1/6}\frac{a}{2} \\ 0, & r < R - 2^{1/6}\frac{a}{2} \end{cases} \quad (6)$$

The dynamics of the position $\mathbf{r}_k$ and orientation φ_k of the kth walker is governed by

$$\dot{\mathbf{r}}_k = v\begin{pmatrix}\cos\varphi_k \\ \sin\varphi_k\end{pmatrix} + \mathbf{F}_k \quad (7)$$

with the force on the kth walker $\mathbf{F}_k = -\nabla_k(U_{\mathrm{WCA}} + U_{\mathrm{con}})$ and

$$\dot{\varphi}_k = \omega_k + \frac{\kappa a^2}{\pi\sigma^2\tau}\sum_{l\in N_k}\sin(\varphi_l - \varphi_k) + \sqrt{2/\tau}\eta_k \quad (8)$$

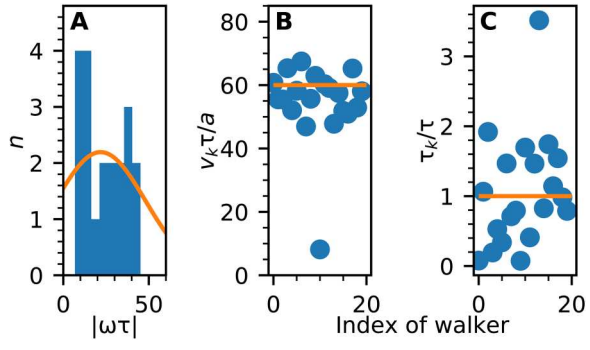

Fig. 8. Walker parameters. (**A**) Distribution of magnitude of angular speeds obtained from experiments (blue histogram) and distribution used in simulations (orange line). (**B**) Reduced propulsion speed and (**C**) correlation time obtained by fitting the measured MSD with Eq. 3. The orange lines indicate the constant values used in the simulations.

As mentioned in the Collision dynamics section, we set $\kappa = 40$ and $\sigma = 1.25a$. We integrate these coupled equations with a time step $\delta t = 10^{-6}\tau$. Under confinement, walkers experience an additional torque

$$\frac{\kappa a^2}{\pi\sigma^2\tau}\cos(\varphi_k - \theta_k) \quad (9)$$

with the wall, where θ_k is defined as the angle between the wall normal going through the position of the kth walker and the positive x axis. This torque aligns walkers along the tangent to the wall.

Supplementary Materials

This PDF file includes:

Supplementary Text
Figs. S1 to S3
Table S1
Legends for movies S1 to S5

Other Supplementary Material for this manuscript includes the following:

Movies S1 to S5

REFERENCES AND NOTES

1. M. Sitti, Voyage of the microrobots. *Nature* **458**, 1121–1122 (2009).
2. E. M. Purcell, Life at low Reynolds number. *Am. J. Phys.* **45**, 3–11 (1977).
3. W. Bialek, *Biophysics* (Princeton Univ. Press, 2012).
4. M. Rubenstein, C. Ahler, R. Nagpal, Kilobot: A low cost scalable robot system for collective behaviors, *Proceedings of the 2012 IEEE International Conference on Robotics and Automation*, Saint Paul, MN, USA, 14–18 May 2012, pp. 3293–3298.
5. G.-Z. Yang, J. Bellingham, P. E. Dupont, P. Fischer, L. Floridi, R. Full, N. Jacobstein, V. Kumar, M. Mc-Nutt, R. Merrifield, B. J. Nelson, B. Scassellati, M. Taddeo, R. Taylor, M. Veloso, Z. L. Wang, R. Wood, The grand challenges of *Science Robotics*. *Sci. Robot.* **3**, eaar7650 (2018).
6. H.-R. Jiang, N. Yoshinaga, M. Sano, Active motion of a Janus particle by self-thermophoresis in a defocused laser beam. *Phys. Rev. Lett.* **105**, 268302 (2010).
7. I. Buttinoni, J. Bialke, F. Kummel, H. Lowen, C. Bechinger, T. Speck, Dynamical clustering and phase separation in suspensions of self-propelled colloidal particles. *Phys. Rev. Lett.* **110**, 238301 (2013).
8. J. R. Howse, R. A. L. Jones, A. J. Ryan, T. Gough, R. Vafabakhsh, R. Golestanian, Self-motile colloidal particles: From directed propulsion to random walk. *Phys. Rev. Lett.* **99**, 048102 (2007).
9. J. Palacci, S. Sacanna, A. P. Steinberg, D. J. Pine, P. M. Chaikin, Living crystals of light-activated colloidal surfers. *Science* **339**, 936–940 (2013).
10. H. R. Vutukuri, M. Lisicki, E. Lauga, J. Vermant, Light-switchable propulsion of active particles with reversible interactions. *Nat. Commun.* **11**, 2628 (2020).
11. J. Yan, M. Han, J. Zhang, C. Xu, E. Luijten, S. Granick, Reconfiguring active particles by electrostatic imbalance. *Nat. Mater.* **15**, 1095–1099 (2016).
12. A. Bricard, J.-B. Caussin, N. Desreumaux, O. Dauchot, D. Bartolo, Emergence of macroscopic directed motion in populations of motile colloids. *Nature* **503**, 95–98 (2013).
13. D. Das, E. Lauga, Active particles powered by quincke rotation in a bulk fluid. *Phys. Rev. Lett.* **122**, 194503 (2019).
14. A. Mauleon-Amieva, M. Mosayebi, J. E. Hallett, F. Turci, T. B. Liverpool, J. S. van Duijneveldt, C. P. Royall, Competing active and passive interactions drive amoebalike crystallites and ordered bands in active colloids. *Phys. Rev. E* **102**, 032609 (2020).
15. V. Sourjik, H. C. Berg, Functional interactions between receptors in bacterial chemotaxis. *Nature* **428**, 437–441 (2004).
16. R. Mesibov, J. Adler, Chemotaxis toward amino acids in Escherichia coli. *J. Bacteriol.* **112**, 315–326 (1972).
17. S. T. Emlen, Migration: Orientation and navigation, in *Avian Biology*, D. Farner and J. King, Eds. (Elsevier, 1975), pp. 129–219.
18. H. H. Wensink, J. Dunkel, S. Heidenreich, K. Drescher, R. E. Goldstein, H. Löwen, J. M. Yeomans, Mesoscale turbulence in living fluids. *Proc. Natl. Acad. Sci. U.S.A.* **109**, 14308–14313 (2012).

19. G. Gompper, R. G. Winkler, T. Speck, A. Solon, C. Nardini, F. Peruani, H. Löwen, R. Golestanian, U. B. Kaupp, L. Alvarez, T. Kiørboe, E. Lauga, W. C. K. Poon, A. DeSimone, S. Muinõs-Landin, A. Fischer, N. A. Soker, F. Cichos, R. Kapral, P. Gaspard, M. Ripoll, F. Sagues, A. Doostmohammadi, J. M. Yeomans, I. S. Aranson, C. Bechinger, H. Stark, C. K. Hemelrijk, F. J. Nedelec, T. Sarkar, T. Aryaksama, M. Lacroix, G. Duclos, V. Yashunsky, P. Silberzan, M. Arroyo, S. Kale, The 2020 motile active matter roadmap. *J. Phys. Condens. Matter* **32**, 193001 (2020).
20. C. F. Lee, Active particles under confinement: Aggregation at the wall and gradient formation inside a channel. *New J. Phys.* **15**, 055007 (2013).
21. H. H. Wensink, H. Löwen, Aggregation of self-propelled colloidal rods near confining walls. *Phys. Rev. E* **78**, 031409 (2008).
22. J. Elgeti, G. Gompper, Wall accumulation of self-propelled spheres. *Europhys. Lett.* **101**, 48003 (2013).
23. M. B. Wan, C. J. Olson Reichhardt, Z. Nussinov, C. Reichhardt, Rectification of swimming bacteria and self-driven particle systems by arrays of asymmetric barriers. *Phys. Rev. Lett.* **101**, 018102 (2008).
24. C. O. Reichhardt, C. Reichhardt, Ratchet effects in active matter systems. *Annu. Rev. Condens. Matter Phys.* **8**, 51–75 (2017).
25. N. Kumar, R. K. Gupta, H. Soni, S. Ramaswamy, A. K. Sood, Trapping and sorting active particles: Motility-induced condensation and smectic defects. *Phys. Rev. E* **99**, 032605 (2019).
26. S. Kim, C. Laschi, B. Trimmer, Soft robotics: A bioinspired evolution in robotics. *Trends Biotechnol.* **31**, 287–294 (2013).
27. M. Cianchetti, C. Laschi, A. Menciassi, P. Dario, Biomedical applications of soft robotics. *Nat. Rev. Mater.* **3**, 143–153 (2018).
28. Y. Fily, A. Baskaran, M. F. Hagan, Dynamics of self-propelled particles under strong confinement. *Soft Matter* **10**, 5609–5617 (2014).
29. L. Giomi, N. Hawley-Weld, L. Mahadevan, Swarming, swirling and stasis in sequestered bristle-bots. *Proc. R. Soc. A.* **469**, 20120637 (2013).
30. B. ten Hagen, S. van Teeffelen, H. Löwen, Brownian motion of a self-propelled particle. *J. Phys. Condens. Matter* **23**, 194119 (2011).
31. M. R. Shaebani, A. Wysocki, R. G. Winkler, G. Gompper, H. Rieger, Computational models for active matter. *Nat. Rev. Phys.* **2**, 181–199 (2020).
32. J. Deseigne, O. Dauchot, H. Chaté, Collective motion of vibrated polar disks. *Phys. Rev. Lett.* **105**, 098001 (2010).
33. C. Scholz, S. Jahanshahi, A. Ldov, H. Löwen, Inertial delay of self-propelled particles. *Nat. Commun.* **9**, 5156 (2018).
34. C. Scholz, M. Engel, T. Pöschel, Rotating robots move collectively and self-organize. *Nat. Commun.* **9**, 931 (2018).
35. O. Dauchot, V. Démery, Dynamics of a self-propelled particle in a harmonic trap. *Phys. Rev. Lett.* **122**, 068002 (2019).
36. M. Leoni, M. Paoluzzi, S. Eldeen, A. Estrada, L. Nguyen, M. Alexandrescu, K. Sherb, W. W. Ahmed, Surfing and crawling macroscopic active particles under strong confinement: Inertial dynamics. *Phys. Rev. Res.* **2**, 043299 (2020).
37. H. Löwen, Inertial effects of self-propelled particles: From active Brownian to active Langevin motion. *J. Chem. Phys.* **152**, 040901 (2020).
38. M. C. Bott, J. M. Brader, R. Wittmann, F. Winterhalter, M. Marechal, A. Sharma, Isotropic-nematic transition of self-propelled rods in three dimensions. *Phys. Rev. E* **98**, 012601 (2018).
39. A. Jayaram, A. Fischer, T. Speck, From scalar to polar active matter: Connecting simulations with meanfield theory. *Phys. Rev. E* **101**, 022602 (2020).
40. T. Vicsek, A. Czirók, E. Ben-Jacob, I. Cohen, O. Shochet, Novel type of phase transition in a system of self-driven particles. *Phys. Rev. Lett.* **75**, 1226–1229 (1995).
41. C. W. Gardiner, *Stochastic Methods: A Handbook for the Natural and Social Sciences* (Springer Series in Synergetics No. 13, Springer, ed. 4, 2009).
42. F. D. C. Farrell, M. C. Marchetti, D. Marenduzzo, J. Tailleur, Pattern formation in self-propelled particles with density-dependent motility. *Phys. Rev. Lett.* **108**, 248101 (2012).
43. D. Levis, I. Pagonabarraga, B. Liebchen, Activity induced synchronization: Mutual flocking and chiral selfsorting. *Phys. Rev. Res.* **1**, 023026 (2019).
44. J. A. Acebrón, L. L. Bonilla, C. J. P. Vicente, F. Ritort, R. Spigler, The Kuramoto model: A simple paradigm for synchronization phenomena. *Rev. Mod. Phys.* **77**, 137–185 (2005).
45. P. de Castro, F. M. Rocha, S. Diles, R. Soto, P. Sollich, Diversity of self-propulsion speeds reduces motility-induced clustering in confined active matter. *Soft Matter* **17**, 9926–9936 (2021).
46. B. Liebchen, D. Levis, Collective behavior of chiral active matter: Pattern formation and enhanced flocking. *Phys. Rev. Lett.* **119**, 058002 (2017).
47. Q.-L. Lei, M. P. Ciamarra, R. Ni, Nonequilibrium strongly hyperuniform fluids of circle active particles with large local density fluctuations. *Sci. Adv.* **5**, eaau7423 (2019).
48. B. Zhang, A. Snezhko, Hyperuniform active chiral fluids with tunable internal structure, Phys. Rev. Lett. 128, 218002 (2022).
49. N. H. P. Nguyen, D. Klotsa, M. Engel, S. C. Glotzer, Emergent collective phenomena in a mixture of hard shapes through active rotation. *Phys. Rev. Lett.* **112**, 075701 (2014).
50. M. Paoluzzi, R. Di Leonardo, M. C. Marchetti, L. Angelani, Shape and displacement fluctuations in soft vesicles filled by active particles. *Sci. Rep.* **6**, 34146 (2016).
51. H. R. Vutukuri, M. Hoore, C. Abaurrea-Velasco, L. van Buren, A. Dutto, T. Auth, D. A. Fedosov, G. Gompper, J. Vermant, Active particles induce large shape deformations in giant lipid vesicles. *Nature* **586**, 52–56 (2020).
52. M. S. E. Peterson, A. Baskaran, M. F. Hagan, Vesicle shape transformations driven by confined active filaments. *Nat. Commun.* **12**, 7247 (2021).
53. J. F. Boudet, J. Lintuvuori, C. Lacouture, T. Barois, A. Deblais, K. Xie, S. Cassagnere, B. Tregon, D. B. Bruckner, J. C. Baret, H. Kellay, From collections of independent, mindless robots to flexible, mobile, and directional superstructures. *Sci. Robot.* **6**, eabd0272 (2021).
54. G. Wang, T. V. Phan, S. Li, M. Wombacher, J. Qu, Y. Peng, G. Chen, D. I. Goldman, S. A. Levin, R. H. Austin, L. Liu, Emergent field-driven robot swarm states. *Phys. Rev. Lett.* **126**, 108002 (2021).
55. S. van Teeffelen, H. Löwen, Dynamics of a Brownian circle swimmer. *Phys. Rev. E* **78**, 020101 (2008).
56. J. D. Weeks, D. Chandler, H. C. Andersen, Role of repulsive forces in determining the equilibrium structure of simple liquids. *J. Chem. Phys.* **54**, 5237–5247 (1971).

Acknowledgments: Computations were performed on the supercomputer MOGON II. **Funding:** We acknowledge funding by the Deutsche Forschungsgemeinschaft (DFG) within collaborative research center TRR 146 (grant no. 404840447). **Author contributions:** P.B. and T.S. designed research. F.S. performed the experiments and simulations, F.S. and A.J. analyzed the data and developed the research hypothesis. All authors contributed to interpreting the data and writing the manuscript. **Competing interests:** The authors declare that they have no competing interests. **Data and materials availability:** All data needed to evaluate the conclusions in the paper are present in the paper and/or the Supplementary Materials.

Submitted 28 October 2022
Accepted 15 March 2023
Published 14 April 2023
10.1126/sciadv.adf5443